Evaluation of the Constant Pressure Panel Method for Supersonic Unsteady Airloads Prediction

Kari Appa* and Michael J. C. Smith†
Northrop Corporation, Hawthorne, California

This paper evaluates the capability of the constant pressure panel method (CPM) code to predict unsteady aerodynamic pressures, lift and moment distributions, and generalized forces for general wing-body configurations in supersonic flow. Stability derivatives are computed and correlated for the X-29 and an oblique wing research aircraft, and flutter analyses are carried out for two wind-tunnel test examples. Most results are shown to correlate well with test or published data. Although the emphasis of this paper is on evaluation, an improvement in the handling of intersecting lifting surfaces is briefly discussed. An attractive feature of the CPM code is that it shares the basic data requirements and computational arrangements of the doublet lattice method. A unified code to predict unsteady subsonic or supersonic airloads has thus been developed.

Introduction

ACCURATE prediction of unsteady aerodynamic loads is an important consideration for the determination of flutter margins, gust loads, and aeroservoelastic effects. In subsonic flow, the doublet lattice method (DLM, Ref. 1) has become an industry-wide accepted analytical tool. In supersonic flow, a similar standard has not emerged, although a number of computational schemes have been reported in the literature.[2-13] Detailed discussions on the relative merits of these methods can be found in Ref. 12. An extension to the harmonic gradient method of Ref. 11 is reported in Ref. 15. This proposes source singularities to represent body components, whereas lifting surface components are represented by a modified version of potential gradients, and also requires calculations in the wake region. The system of equations first solves for the field variables (sources and potential gradients), which are then employed to calculate the potentials and subsequently the pressure distribution. On the contrary, the present constant pressure panel method (CPM) employs acceleration potentials (i.e., pressure) to represent both body and lifting surface components. Hence, a direct relationship between the pressure and the normal velocity on lifting surfaces is developed. A numerical integration scheme using finite elements is employed to determine the pressure distribution on interfering surfaces. Another key advantage of the CPM is that it is similar to the doublet lattice method in terms of basic data input and computational arrangement. Hence, a unified code to predict unsteady subsonic or supersonic airloads can be achieved. In fact, this has been done in the NASA Ames version of the FASTEX code,[14] operational at the Dryden Flight Research Facility, as well as in the ASTROS code.[16]

The purpose of this paper is to evaluate the capability of the CPM code to predict a variety of aerodynamic and aeroelastic quantities on general wing-body combinations. In previous studies, correlations in terms of pressure and integrated loads have been demonstrated using simple planforms. The present study compares results with previous studies in order to demonstrate the accuracy of the method. In addition, results from other arbitrary wing-body combinations are presented without correlation to serve as a data base for other investigators.

Presented as Paper 88-2282 at the AIAA/ASME/ASCE/AHS 29th Structures, Structural Dynamics and Materials Conference, April 18–20, 1988; received June 20, 1988; revision received Feb. 7, 1989.

*Senior Technical Specialist, Aircraft Division.
†Engineering Specialist, Aircraft Division. Member AIAA.

Modified Computational Procedure

Before presenting the comparison results, a brief discussion of an enhancement to CPM is given. In Ref. 12, the computation of the normal velocity at a receiving element i, due to a uniform pressure distribution on panel j, was given by

$$W_{ij} = \frac{1}{2\pi}\int_{\eta_L}^{\eta_U}\left(C_1 w_1 + C_2 \frac{1}{r}\frac{\partial w_1}{\partial r}\right)\mathrm{d}\eta \tag{1}$$

where

$$w_1 = \frac{F(\eta)}{r^2}$$

$$C_1 = l_Z l_{Z_0} + l_y l_{y_0}$$

$$C_2 = [\zeta^2 l_z l_{z_0} + \eta^2 l_y l_{y_0} + \eta\zeta(l_y l_{z_0} + l_z l_{y_0})]$$

$$r^2 = \eta^2 + \zeta^2$$

Also,

$$\begin{aligned} F(\eta) = {} & \left[\frac{\exp(-ik'M\xi)\,\sin k'R}{k'}\right]_{\xi_L}^{\xi_U} \\ & + iM\int_{\xi_L}^{\xi_U}\exp(-ik'M\xi)\,\sin k'R\,\mathrm{d}\xi \\ & + \int_{\xi_L}^{\xi_U}\frac{1}{2}\exp(-ik\xi)\Big(\delta\{\exp[-i(k/\beta^2) \\ & \times(\xi - MR)] - 1\} \\ & + \{1 - \exp[-i(k/\beta^2)(\xi + MR)]\} \\ & + ikr\sum_{m=1}^{m=N} a_m \\ & \times\{\exp[-2^m b(\xi + MR)/\beta^2 r] \\ & \times\exp[-i(k/\beta^2)(\xi + MR)] - 1\}/D_1 \\ & + \delta\{1 - \exp[-2^m b|\xi - MR|/\beta^2 r] \\ & \times\exp[-i(k/\beta^2)(\xi - MR)]\}/D_2\Big)\mathrm{d}\xi \end{aligned} \tag{2}$$

where

$$R^2 = \xi^2 - \beta^2 r^2$$

$$k = \frac{\omega l}{V} = \text{reduced frequency}$$

(l is a characteristic length, and V is the freestream velocity)

$$k' = \frac{kM}{\beta^2}$$

$$\xi = X_0 - X$$

$$\eta = Y_0 - Y$$

$$\zeta = Z_0 - Z$$

$$\beta = \sqrt{M^2 - 1}$$

$$\delta = \text{sign}(\xi - MR)$$

M = Mach number

X_0, Y_0, Z_0 denote the coordinates of a receiving point while X, Y, Z denote the coordinates of the field point within an influencing element. Any further definitions for $F(\eta)$ may be found in Ref. 12.

$F(\eta)$ is an analytic function resulting from the chordwise integration of the supersonic kernel function at spanwise station of the influencing element. This function vanishes on the Mach boundary as well as outside the domain of influence. The terms l_y, l_z and l_{y_0}, l_{z_0} denote the direction cosines of the influencing and the receiving elements, respectively. A numerical evaluation of the derivative $(\partial w_1)/(\partial r)$ was used in Ref. 12. However, for intersecting panels this procedure was found to be numerically unsatisfactory. Hence, an alternative algorithm, defined by the following expression, was adopted:

$$W_{ij} = \frac{1}{2\pi} \int_{\eta_L}^{\eta_U} \left[\frac{C_1 F(\eta)}{r^2} + \frac{C_2 \left\{ r \dfrac{\partial F(\eta)}{\partial r} - 2F(\eta) \right\}}{r^4} \right] d\eta \quad (3)$$

The derivative of the function $F(\eta)$ with respect to r can be computed numerically since it is analytic. The dipole and quadrupole singularities are evaluated by analytical methods by expressing the numerators as quadratic polynomials in η. These changes improve the computational stability of the CPM code.

Correlation Studies

To demonstrate the capability and the accuracy of the CPM code, several test cases, including an isolated wing and interfering wing-tail, T-tails, symmetric and asymmetric wing-body combinations, were considered. The computed pressures, lift and moment distributions, stability derivatives, generalized aerodynamic forces, and flutter solutions have been correlated, where possible, with known data either from other analytical methods or wind-tunnel tests.

Steady Data

Steady Pressure Distribution on the Cornell Flutter Model

The flutter model shown in Fig. 1 was tested in a Cornell Aeronautical Laboratories wind tunnel.[17] The U.S. Air Force has recently used this model in several studies and supplied results to Northrop for comparative purposes.[18] The planform was represented in CPM by 20 spanwise panels and 10 chordwise panels. Computations were performed at two Mach numbers, namely, $M = 1.135$ and 1.2. The pressure distributions predicted by CPM at 75% of the wing span for these two Mach numbers, together with data from Ref. 18, are shown in Figs. 2 and 3.

The solid lines in these figures denote the pressure distributions predicted by the Mach box method of Ref. 5, whereas the data denoted by the circular and square symbols were obtained from the linear and nonlinear versions of XTRAN3S,[19] respectively. Near the leading edge, the CPM predicted data correlate well with the linear model of XTRAN3S, while near the trailing edge, the CPM results are seen to be the average of the linear and nonlinear data. The unsmoothed Mach box data shows an oscillatory distribution whose average is somewhat above other results.

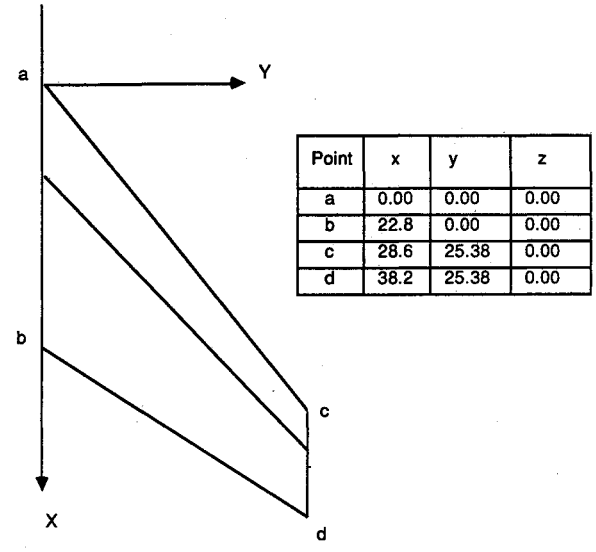

Point	x	y	z
a	0.00	0.00	0.00
b	22.8	0.00	0.00
c	28.6	25.38	0.00
d	38.2	25.38	0.00

Fig. 1 Planform of the Cornell Flutter Model.

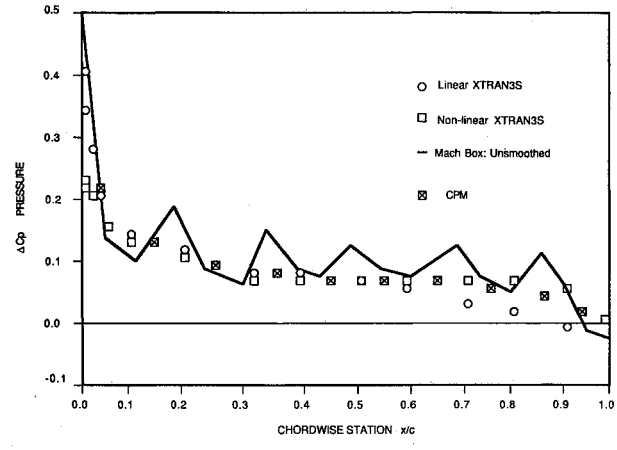

Fig. 2 Chordwise pressure distribution on the Cornell wing, $M = 1.1.35, y/b = 0.75$.

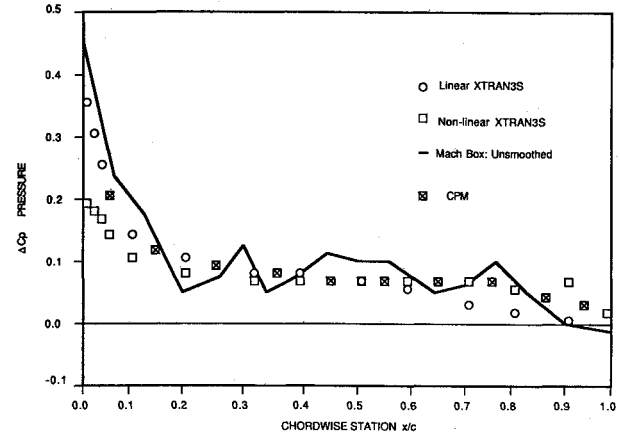

Fig. 3 Chordwise pressure distribution on the Cornell wing, $M = 1.2, y/b = 0.75$.

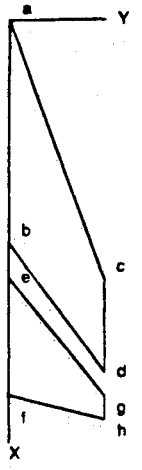

CASE		x	y	z
1. COPLANAR	a	0.00	0.00	0.00
	b	2.25	0.00	0.00
	c	2.75	1.00	0.00
	d	3.70	1.00	0.00
	e	2.70	0.00	0.00
	f	4.00	0.00	0.00
	g	3.90	1.00	0.00
	h	4.25	1.00	0.00
2. TAIL 30DEG DIHEDRAL	g'	3.90	0.866	0.5
	h'	4.25	0.866	0.5

MODE	WING	TAIL
WING TWIST	y(x-2.25 |y| -0.85)	0.0
WING BENDING	y|y|	0.0
TAIL PITCH	0.0	x-3.35
TAIL ROLL	0.0	y

Fig. 4 AGARD wing tail configuration.

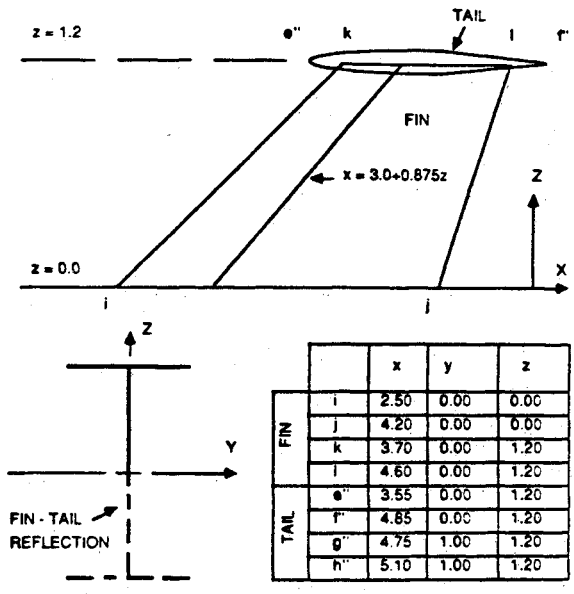

		x	y	z
FIN	i	2.50	0.00	0.00
	j	4.20	0.00	0.00
	k	3.70	0.00	1.20
	l	4.60	0.00	1.20
TAIL	e"	3.55	0.00	1.20
	f"	4.85	0.00	1.20
	g"	4.75	1.00	1.20
	h"	5.10	1.00	1.20

MODE	FIN	TAIL
FIN BENDING	z^2	0.0
FIN TWIST	|z|(x-0.875|z|-3.0)	0.0
TAIL ROLL	0.0	y

Fig. 5 AGARD horizontal tail-vertical fin. Configuration (configuration is reflected about the xy-plane).

Table 1 Correlation of the steady lift coefficient for the AGARD wing-tail configuration

Mach number	Lift coefficient	Tail $z = 0.0$ Dihedral = 0 USSAERO	Tail $z = 0.0$ Dihedral = 0 CPM	Tail $z = 0.6$ Dihedral = 0 USSAERO	Tail $z = 0.6$ Dihedral = 0 CPM	Tail $z = 0.0$ Tail 30-deg dihedral USSAERO	Tail $z = 0.0$ Tail 30-deg dihedral CPM
1.2	CL wing	5.594	5.189	5.397	5.203	5.488	5.199
	CL tail	−4.786	−4.541	−1.447	−1.531	−1.777	−1.782
1.6	CL wing	5.593	5.224	5.499	5.224	5.593	5.224
	CL tail	−3.335	−3.103	−1.284	−1.124	−1.195	−1.018
3.0	CL wing	4.493	4.254	4.493	4.254	4.493	4.254
	CL tail	−1.042	−1.051	−1.556	−1.256	−0.674	−0.528

Wing incidence = 1 deg.
Tail incidence = 0 deg.

Steady Lift

Figures 4 and 5 show standard AGARD wing-tail and fin-tail configurations for which CPM-predicted steady forces are compared with results obtained from the USSAERO code.[20] Table 1 shows the lift coefficients on the wing and tail in steady symmetric flow at Mach numbers $M = 1.2$, 1.6, and 3.0. Tail positions include $Z = 0.0$, 0.6, and, at $Z = 0.0$, a dihedral angle of 30 deg (i.e., planar, noncoplanar, and intersecting). The CPM-predicted lift coefficients agree reasonably well with results of USSAERO. However, it is noted that the CPM results are slightly lower than those of USSAERO.

Unsteady Data

Pressure and Force Distributions

To verify the reliability of the CPM code, a number of standard AGARD wing-tail configurations were analyzed. The pressure and force distributions in the unsteady cases were compared with the results of the Mach box method reported in Refs. 18 and 21. For the coplanar and the parallel wing-tail configurations, the CPM-predicted results were found to be in reasonable agreement with the referenced data. Typical force distributions on the tail for the coplanar case are shown in Fig. 6, which indicates good agreement with the Mach box data of Ref. 21.

However, the predicted results for the 30-deg dihedral tail configuration did not match the smoothed Mach box results very well. Figures 7 and 8 show the CPM and the Mach box method computed pressures, as well as spanwise lift and moment distributions on the wing and tail, respectively. In Fig. 7, significant differences were found in the real components of the pressure and lift distributions, and in the imaginary components of the moment distributions. There appears to be an inconsistency in the imaginary component of the moment, since the imaginary components of the pressure and lift distributions are in reasonable agreement. Similarly, the real component of the moment shows reasonable correlation with the Mach box results while the real components of the pressure and lift distributions disagree. Figure 8 shows similar data for the tail component. Although the distributions are similar, the magnitudes of the data differ significantly. In general, CPM seems to predict higher tail loads than the Mach box method. It is hoped that this lack of agreement can be resolved by results from other investigators and methods.

Generalized Forces on The Wing-Tail Configurations

The generalized aerodynamic forces computed for the AGARD wing-tail configuration deforming in antisymmetric modes (such as wing twist, wing bending, tail pitch, and tail rolling) are shown in Table 2.

The first set in the table compares the CPM-computed data for the coplanar configuration with the Mach box method reported in Ref. 21. The generalized forces for the wing- and tail-deformation modes are in good agreement with each other except for the wing-twist/wing-twist modal combination. Similar data for the 30-deg dihedral tail configuration are shown in the second part of the table. No other source was found to correlate with these data; however, this may serve as information for other investigators.

Generalized Forces on the Tail-Fin Configuration

The top mounted AGARD tail-fin (T-tail) shown in Fig. 5 was used to compute the generalized forces for a configuration with intersecting surfaces. Three antisymmetric modes, namely, fin bending, fin twisting, and tail rolling, were employed. Analyzes were performed using 10 chordwise and 15 spanwise panel distributions on each component. The generalized forces computed with and without ground symmetry (reflection) did not show any significant differences. Ground symmetry was chosen in order to correspond with the model of Ref. 22. The results presented in Table 3 represent the loads on one half of the T-tail configuration.

For the steady case, the generalized forces for the fin-twisting mode are shown in the third column of Table 3. The fin-bending (Q21) and fin-twisting (Q22) moments agree reasonably well with those of Refs. 8 and 9, whereas Ref. 22 predicts much higher loads. However, the tail-bending moment (Q23) computed by the present method is seen to be nearly twice as much as that predicted by Refs. 8 and 9. It appears there is a point of confusion in the definition of the

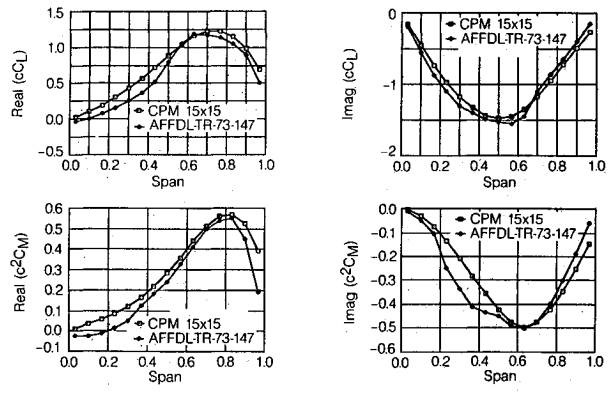

Fig. 6 Comparison of the lift (cC_L) and moment (c^2C_M) distributions on the tail, due to antisymmetric wing twist in the AGARD wing-tail coplanar configuration, $M = 1.2$, $k = 1.5$, $z = 0.0$.

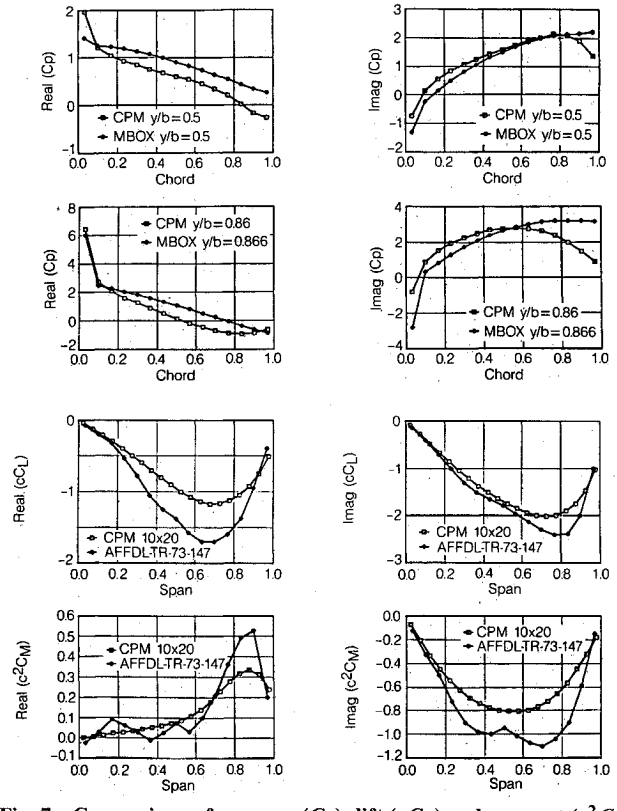

Fig. 7 Comparison of pressure (C_p), lift (cC_L) and moment (c^2C_M) distributions due to antisymmetric wing twist on the wing in the AGARD wing-tail (tail 30 deg dihedral) configuration, $M = 1.2$, $k = 1.5$.

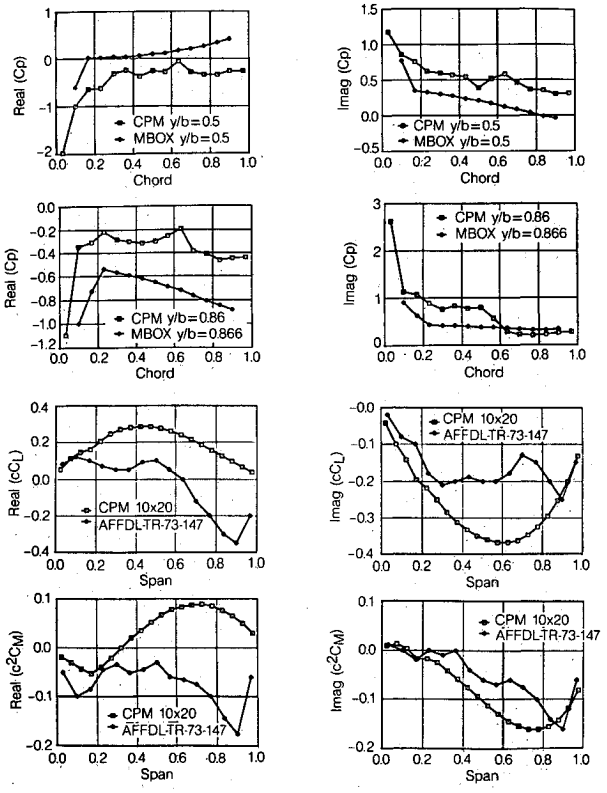

Fig. 8 Comparison of pressure (C_p), lift (cC_L) and moment (c^2C_M) distributions due to antisymmetric wing twist on the tail in the AGARD wing-tail (tail 30 deg dihedral) configuration, $M = 1.2$, $k = 1.5$.

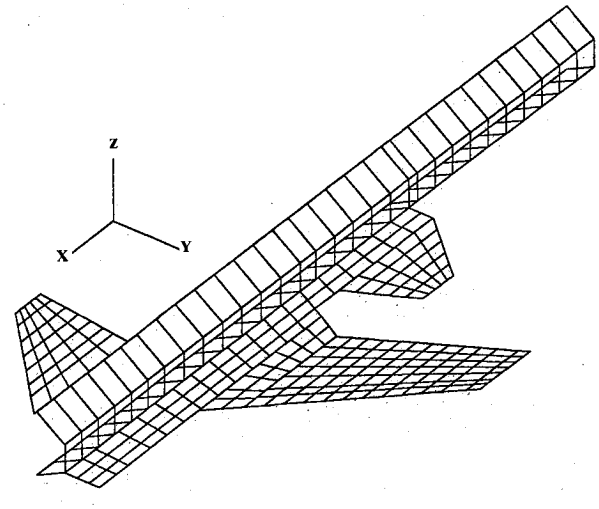

Fig. 9 X-29 modelling for unsteady airloads predictions.

Table 2 Correlation of generalized force coefficients for the AGARD wing-tail configuration

AGARD	Coplanar	$M = 1.2$	$K = 1.5$		
Generalized force coeff. in	Due to pressure in	CPM (15 × 20)		Mach box (Ref. 21)	
Wing twist	Wing twist	−0.1279	0.2023	−0.0931	0.2675
Wing bend	Wing twist	−0.3001	0.4024	0.4040	0.4221
Wing twist	Wing bend	−0.1303	−0.02	−0.1491	0.0044
Wing bend	Wing bend	−0.3081	0.2417	−0.3009	0.2772
Tail pitch	Wing twist	−0.2569	0.185	−0.2390	0.2017
Tail roll	Wing twist	−0.4049	0.3053	−0.4149	0.3175
Tail pitch	Wing bend	−0.2996	−0.0209	−0.3141	−0.0046
Tail roll	Wing bend	−0.4503	−0.0131	−0.4632	0.0015
Tail pitch	Tail pitch	0.4825	0.6257	0.5005	0.6388
Tail roll	Tail pitch	0.9517	0.5702	1.0239	0.565
Tail pitch	Tail roll	−0.1474	0.2941	−0.1467	0.2911
Tail roll	Tail roll	−0.097	0.4711	−0.0982	0.4828
AGARD	Tail 30 deg	Dihedral	$M = 1.2$		
Generalized force coeff. in	Due to pressure in	CPM (10 × 20) $K = 0$		CPM (10 × 20) $K = 1.5$	
Wing twist	Wing twist	−0.0539	—	−0.0944	0.2951
Wing bend	Wing twist	0.2276	—	0.3029	0.5496
Wing twist	Wing bend			−0.1244	−0.0104
Wing bend	Wing bend			−0.2730	0.3568
Tail pitch	Wing twist	−0.0569	—	−0.0303	0.0832
Tail roll	Wing twist	−0.1512	—	−0.0882	0.1428
Tail pitch	Wing bend			−0.0677	0.0123
Tail roll	Wing bend			−0.1151	0.0176
Tail pitch	Tail pitch	0.2461	—	0.3327	0.6924
Tail roll	Tail pitch	0.5654	—	0.6668	0.6472
Tail pitch	Tail roll			−0.1128	0.3235
Tail roll	Tail roll			−0.07849	0.5156

forces among the methods referenced. Reference 22 might be referring to the total forces including the components in the plane of symmetry about $y = 0$, as well as the reflection, whereas Refs. 8 and 9 include the forces on the fin and one side of the tail component.

Unsteady data are shown in column 4 of Table 3. It is noticed that the forces predicted by the CPM code generally agree with those of Refs. 8 and 9, except for Q13, Q23, and Q32. However, it is interesting to note that the Q23 seems to agree with Ref. 22. This indicates that there is some inconsistency in the definition of the forces on the fin and tail components. This discrepancy needs to be clarified.

Comparison of the Stability Derivatives

Correlation of the stability derivatives on two research aircraft, namely, the X-29 and an oblique wing configured aircraft, was performed under a contract from the NASA Ames, Dryden Flight Research Facility.

Stability Derivatives of the X-29 Aircraft

The X-29 forward swept wing aircraft was modeled as shown in Fig. 9 with 90 body panels and 211 lifting surface panels. The longitudinal and lateral stability derivatives were computed at Mach numbers $M = 1.05$ and 1.2.

Table 4 shows a comparison between the rigid longitudinal stability derivatives computed by CPM and those of Ref. 23. The lift curve slope C_{L_α} compares very well, whereas the pitching moment coefficient C_{M_α} shows some difference. However, since the aerodynamic center is very close to the reference pitch axis, a small variation in the aerodynamic center would account for a large variation in the pitching moment. Thus, a more meaningful item of comparison would be the location of the aerodynamic center itself. The variation in the location of the aerodynamic center between the present prediction and the reference data is less than 2.3% of the mean aerodynamic chord. The lift and moment derivatives due to canard, strake, and flap are all seen to be in reasonable agreement with those of Ref. 23, except for the canard lift coefficient at $M = 1.05$, which is approximately half that reported in Ref. 23. This variation may arise from the Mach wave interference with the fuselage intake, which was not included in the present analysis.

The dynamic derivatives $C_{M_{\dot\alpha}}$, C_{L_q}, and C_{M_q} also agree reasonably well with the referenced data, while the $C_{L_{\dot\alpha}}$ term is significantly different both in sign and magnitude. In order to examine this discrepancy, a parabolic displacement mode was used to calculate the C_{L_q} and C_{M_q} terms. The C_{L_q} and C_{M_q} values determined in this manner agreed exactly with the results obtained from the unsteady data (which are dependent on $C_{L_{\dot\alpha}}$). Hence, the $C_{L_{\dot\alpha}}$ value predicted by CPM is considered to be reasonable.

Table 5 shows a similar comparison of the lateral stability derivatives. Once again, the rate and control derivatives are seen to be in reasonable agreement with the referenced data except for the derivatives $C_{n_{\dot\beta}}$, C_{n_β}, C_{n_r}, and C_{n_p}.

In general, the CPM-predicted X-29 stability derivatives are seen to be in reasonable agreement with the data presented in Ref. 23.

Stability Derivatives of an Oblique Wing Research Aircraft

To verify the asymmetric capability of the CPM/FASTEX code, an analysis was performed on the 200-ft^2 (wing area) oblique-wing research aircraft to determine the stability derivatives of the aircraft. The complete aircraft was represented in CPM by 308 elements, with 180 elements on the body, 68 elements on the wing, 30 elements on the horizontal

Table 3 Correlation of the generalized force coefficients for the AGARD tail-fin configuration, z tail = 1.2, $M = 1.6$

Method	Q_{ij}	$k = 0$ MOD(Q)	$k = 1.5$ MOD(Q)	$k = 1.5$ ARG(Q), deg
Ref. 8	11		0.8186	89.35
Ref. 9	11		0.7801	90.92
Ref. 22	11		7.1943	79.27
CPM (Present)	11		0.8035	92.25
Ref. 8	12		0.0887	128.57
Ref. 9	12		0.0905	131.93
Ref. 22	12		0.2094	71.51
CPM (Present)	12		0.1075	129.80
Ref. 8	13		0.1053	−63.29
Ref. 9	13		0.1898	72.84
Ref. 22	13		2.5818	79.67
CPM (Present)	13		0.3145	15.61
Ref. 8	21	0.7948	0.7115	13.23
Ref. 9	21	0.8089	0.686	18.22
Ref. 22	21	2.7068	1.5532	−24.23
CPM (Present)	21	0.7845	0.71	18.70
Ref. 8		0.0807	0.26	63.36
Ref. 9		0.097	0.2671	67.30
Ref. 22		0.3511	0.3924	43.99
CPM (Present)		0.0978	0.26	63.17
Ref. 8	23	0.1828	0.047	−166.97
Ref. 9	23	0.2258	0.1397	177.11
Ref. 22	23	0.5621	0.3766	−68.31
CPM (Present)	23	0.437	0.2983	−69.40
Ref. 8	31		0.0954	61.86
Ref. 9	31		0.0873	64.92
Ref. 22	31		2.4391	87.06
CPM (Present)	31		0.051	59.22
REf. 8	32		0.0316	48.18
Ref. 9	32		0.1812	7.90
Ref. 22	32		0.0238	27.75
CPM (Present)	32		0.016	51.33
Ref. 8	33		0.7177	88.47
Ref. 9	33		0.6686	89.79
Ref. 22	33		1.0056	88.01
CPM (Present)	33		0.6995	88.35

MODES: 1) fin bending; 2) fin twisting; and 3) tail rolling. References 8 and 9 do not consider fin-tail reflection.

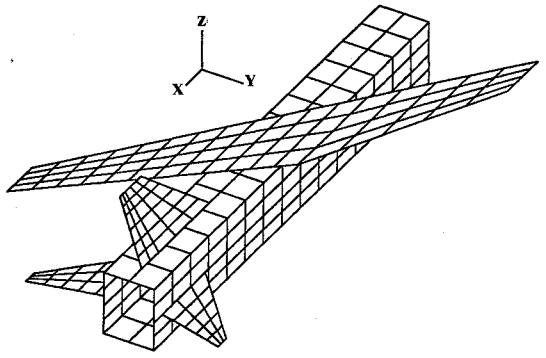

Fig. 10 Oblique wing research aircraft modeling for unsteady airloads prediction.

tail, and 30 elements on the vertical fin (Fig. 10). It would be desirable to represent the total aircraft by a minimum of 600 elements but FASTEX imposes a limit of 320 elements. To determine the stability derivatives, eight displacement modes were used, representing five rigid-body modes and three control surface deflections. The wing rotates above the fuselage about a pivot point. There is a slight gap between the fuselage and the wing at the pivot joint. The wing was set at a sweep angle of 55 deg and a dihedral angle of 5 deg. No streamwise inclination of the wing was considered because the FASTEX

Table 4 X-29 longitudinal stability derivatives (rigid aircraft)

	$M = 1.05$		$M = 1.2$	
	Reference 23	Present (CPM)	Reference 23	Present (CPM)
A/C Pitch*:				
C_{L_α}	0.1073	0.0982	0.0971	0.097
C_{M_α}	0.0156	0.0125	0.0087	0.0068
Canard:				
$C_{L_{\delta c}}$	0.0118	0.0067	0.0099	0.0102
$C_{M_{\delta c}}$	0.0158	0.0155	0.0143	0.0139
Strake:				
$C_{L_{\delta s}}$	0.0029	0.0032	0.0039	0.0027
$C_{M_{\delta s}}$	−0.0051	−0.0075	−0.0062	−0.0063
Flap:				
$C_{L_{\delta f}}$	0.0154	0.0197	0.015	0.0162
$C_{M_{\delta f}}$	−0.0121	−0.0135	−0.0139	−0.0132
$C_{L_{\dot\alpha}}$	0.4165	−11.138	0.3854	−7.896
$C_{M_{\dot\alpha}}$	−1.504	−2.94	−1.527	−1.57
C_{L_q}	7.49	6.483	6.145	4.736
C_{M_q}	−9.568	−9.123	−8.727	−8.863
*Center of pressure (relative to pitch axis):				
X_{cp} (in.)	12.6	11.03	7.765	6.075

Reference area = 26,640 in.^{2}; Reference chord = 86.67 in.; and Reference span = 326.4 in.
Aircraft pitch axis: $X_0 = 448.77$ in., $Z_0 = 61.0$ in.
Canard pitch axis: $X_0 = 372.2$ in., $Z_0 = 61.0$ in.
Dynamic derivatives are per radian, whereas all others are per degree.

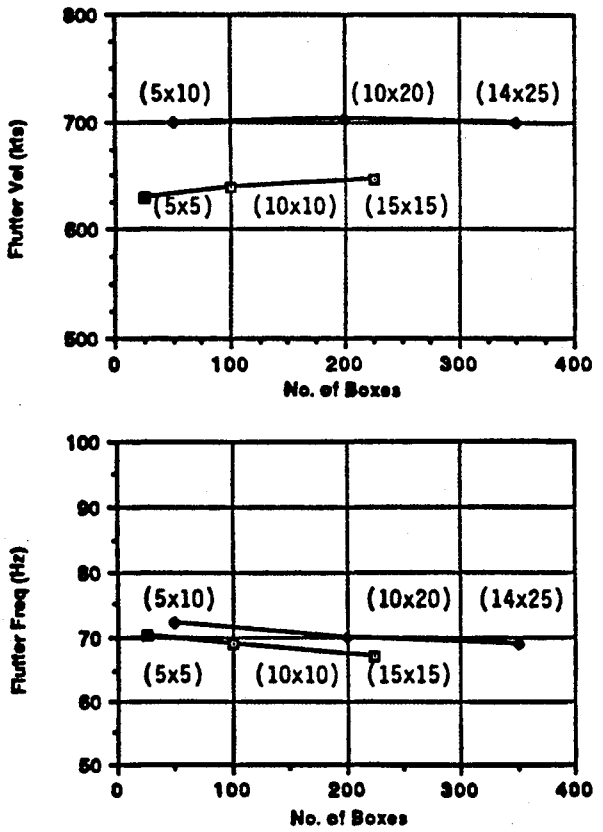

Fig. 11 Flutter speed and frequency vs number of boxes used in the CPM code (Cornell wing).

code employs linearized boundary conditions, which uncouple the incidence and sideslip angles, as discussed in Ref. 14.

Table 6 compares the stability derivatives computed for this configuration using the CPM code with data reported in Ref. 24. The rotary derivatives were reportedly obtained by theo-

Table 5 X-29 lateral stability derivatives (rigid A/C)

	$M = 1.05$		$M = 1.2$	
	Reference 23	Present (CPM)	Reference 23	Present (CPM)
C_{Y_β}	−0.0202	−0.0205	−0.0215	−0.0196
C_{l_β}	−0.0016	−0.0028	−0.0019	−0.0026
C_{n_β}	0.0044	0.0089	0.0049	0.0086
$C_{Y_{\dot\beta}}$	——	−0.0023	——	0.0273
$C_{l_{\dot\beta}}$	——	0.0739	——	0.0469
$C_{n_{\dot\beta}}$	0.0054	−0.2197	0.006	−0.2279
C_{Y_r}	——	1.5402	——	1.4534
C_{l_r}	0.237	0.2559	0.2207	0.2386
C_{n_r}	−0.2563	−0.9648	−0.469	−0.8851
C_{l_p}	−0.4723	−0.4351	−0.515	−0.4659
C_{n_p}	0.0484	0.0659	0.0658	0.0218
$C_{Y_{\delta a}}$	−0.0062	−0.0039	−0.0059	−0.0036
$C_{l_{\delta a}}$	0.002	0.0016	0.0013	0.0014
$C_{n_{\delta a}}$	0.0012	0.002	0.0017	0.0019
$C_{Y_{\delta r}}$	0.0028	0.0031	0.0016	0.0019
$C_{l_{\delta r}}$	0.00056	0.00071	0.0003	0.00045
$C_{n_{\delta r}}$	−0.0017	−0.0021	−0.0011	−0.0013

Reference area = 26,640 in.^{2}; Reference chord = 86.67 in.; and Reference span = 326.4 in.
Aircraft yaw axis: $X_0 = 448.77$ in., $Y_0 = 0.0$ in.
Dynamic derivatives are per radian, whereas all others are per degree.

Table 6 Stability derivatives of oblique wing research aircraft (rigid aircraft); Mach no. = 1.2)

	Rolling moment	Pitching moment	Yawing moment	Lift	Side force	Source
Roll rate	−0.154	1.988	0.0928	0.1748	−0.39	Ref. 24
$(pb/2V)$, rad/s	−0.155	1.616	0.1374	−0.0067	−0.328	CPM
Pitch rate	1.257	−98.07	0.539	16.702	0.18	Ref. 24
$(qc/2V)$, rad/s	−0.0436	−107.84	0.3264	21.22	−0.9914	CPM
Yaw rate	0.1627	−0.0223	−0.875	0.115	2.02	Ref. 24
$(rb/2V)$, rad/s	0.1808	0.1853	−0.678	0.085	2.174	CPM
alpha	0.0985	−4.749	−0.0908	4.943	−0.365	Ref. 24
α, rad	0.1098	−3.768	−0.0395	4.204	0.2208	CPM
beta	−0.123	1.191	0.3396	−0.446	−2.139	Ref. 24
β, rad	−0.211	0.7339	0.4544	−0.2299	−1.927	CPM
left horizontal	0.0397	−2.06	0.0379	0.4536	−0.0882	Ref. 24
δ_{lh}, rad	0.0596	−2.569	0.00003	0.6006	0.00007	CPM
right horizontal	−0.0392	−2.06	−0.0378	0.4536	0.0882	Ref. 24
δ_{rh}, rad	−0.0597	−2.569	−0.00003	0.6006	−0.00007	CPM
Rudder	0.0165	0.033	−0.068	0	0.1501	Ref. 24
δ_r, rad	0.066	0.0029	−0.2261	−0.0004	0.4744	CPM

Reference area = 200 ft^2; Reference chord = 4.778 ft; and Reference span = 45.12 ft.
Aircraft pitch axis: $X_0 = 454.0$ in., $Z_0 = 100.0$ in.
Aircraft yaw axis: $X_0 = 454.0$ in., $Y_0 = 0.0$ in.
Horizontal tail pitch axis: $X_0 = 663.501$ in., $Z_0 = 92.0$ in.
$C_{N_\alpha} = 0.2254$ (CPM) and $C_{m_{\dot\alpha}} = -1.037$ (CPM)

POINT	X (ins)	Y (ins)
a	0.0	0.0
b	46.362	0.0
c	31.866	30.0
d	46.362	30.0

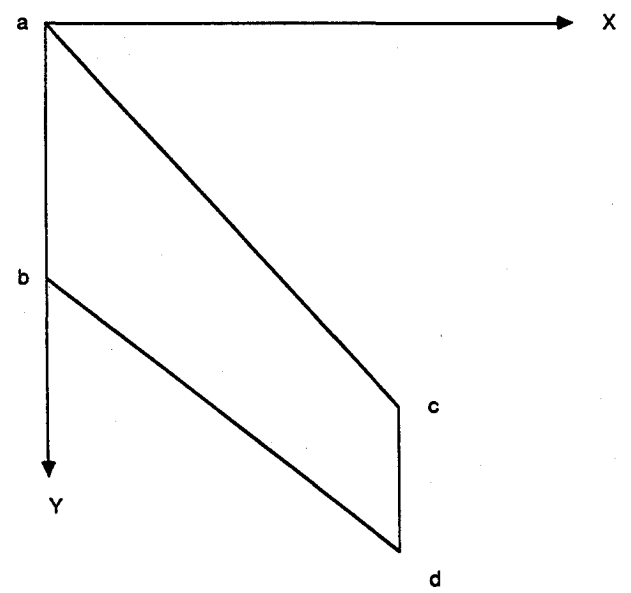

Fig. 12 Planform of weakened 45 swept wing (model 3) of ref. 25.

Table 7 Cornell wing-flutter analysis and test correlation

Model	4	5
Mach	1.098	1.135
ρ/ρ_o	0.2481	0.2607
$V_{f_{\text{exp}}}$	708	717
$V_{f\text{calc}}$ (CPM)	705	736
$\omega_{f_{\text{exp}}}$	69	63
$\omega_{f\text{calc}}$ (CPM)	70	68

retical means, whereas the static derivatives were obtained from wind-tunnel tests. Although a simplified model was used, the direct derivatives, except for rudder effectiveness, are seen to agree reasonably well with those of Ref. 24. The cross derivatives, such as side force due to pitch rate, pitching moment due to side slip, and rolling moment due to pitch rate, show significant differences. The discrepancy associated with the rudder effectiveness may arise from a) simplified modeling, and/or b) viscous and nonlinear effects that are neglected in the potential theory applied.

Flutter Analyses

To verify the accuracy of the flutter-speed predictions, correlation studies were made with two wind-tunnel flutter tests. In the first, the wind-tunnel model (Fig. 1) described in Ref. 17 was represented structurally by three vibration modes. The CPM predicted flutter speeds and corresponding frequencies for this analysis, using various number of boxes, but essentially only two values of nominal panel aspect ratio (1.56 for the 5 chordwise × 10 spanwise, 10 × 20 and 14 × 25 panel arrangements, and 3.13 for the 5 × 5, 10 × 10, and 15 × 15 panel arrangements) are shown in Fig. 11. For a given nominal panel aspect ratio, convergence is seen to be very rapid. The predicted flutter speeds with a 10 chordwise by 20 spanwise box arrangement are compared with the experimental data of Ref. 18 in Table 7. For the density ratio $\rho/\rho_0 = 0.2481$, the predicted flutter speed is about 0.42% conservative, and for the density ratio $\rho/\rho_0 = 0.2607$, it is about 2.65% unconservative. These results, for the lower nominal aspect ratio arrangement, show good correlation with test data. The reason for this being that, in supersonic flow, the domain of influence (the region defined by the forward Mach cone) is reduced for the larger aspect ratio

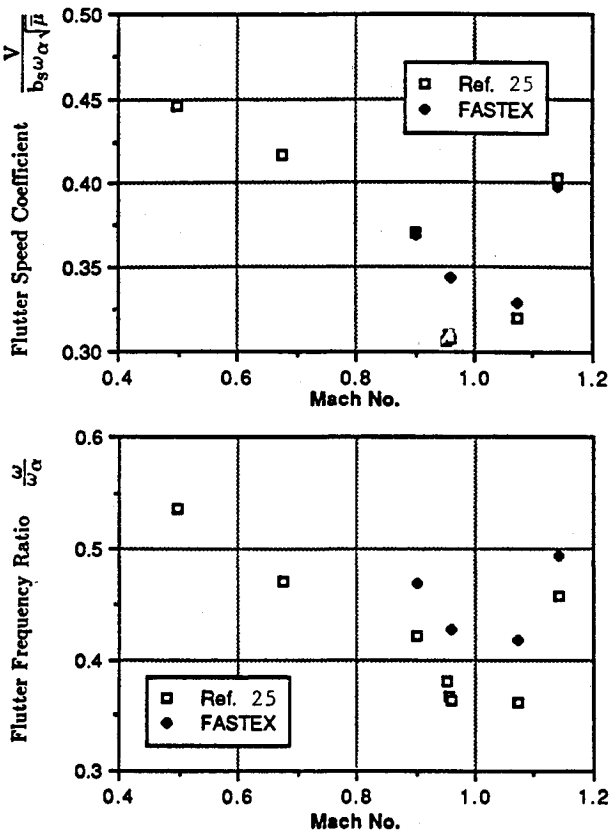

Fig. 13 Flutter speed coefficient and frequency ratio vs Mach number for the weakened 45 swept wing (model 3) of Ref. 25.

element, and a large portion of the element does not contribute to the downwash. It is thus suggested that the panel aspect ratio be such that the Mach lines intersect the side edges of the panel.

The second flutter analysis was carried out (in air) on a 45-deg swept wing (model 3) of Ref. 25, using the five mode shapes developed for this model in Ref. 26. A planform of the model is given in Fig. 12. Results of this analysis are presented in Fig. 13. In this instance, the FASTEX code was exercised subsonically and supersonically. The supersonic results are based on the CPM method and are seen to correspond almost exactly with the reported experimental values of flutter-speed coefficient. It is significant that such good results were obtained, even for the Mach 1.07 case.

Conclusions and Recommendations

The constant pressure panel method has been integrated into the existing doublet lattice code, so that a unified code is available for the determination of unsteady airloads in subsonic and supersonic Mach number ranges. The supersonic CPM code accounts for body interference effects using lifting surface panels lying parallel to the streamlines. However, to account for truly blended wing-body configurations, the CPM method needs to be extended to account for the streamwise inclination of lifting elements.

The CPM code has been exercised using several configurations ranging from simple wing planforms to interfering wing-body configurations. The predicted data in terms of pressures, lift and moment distributions, generalized forces, and stability derivatives have been correlated with known data. Overall agreement is seen to be good. However, in the case of interfering wing surfaces, oscillatory data correlation is limited to a single source (i.e., the Mach box method), due to lack of available data from other methods (except for the T-tail example). The data presented in this paper can serve as a source for further correlation by other investigators. The reported flutter solution shows excellent agreement with test data. However, additional examples using interfering surfaces need to be evaluated.

Acknowledgments

The data presented in this report were generated as part of Northrop's independent research and development activity as well as Contract NAS2-12597, "The Integration of a Supersonic Unsteady Aerodynamic Code into the NASA FASTEX System," for the NASA Ames Dryden Flight Research Facility, for which Dr. K. K. Gupta was the technical monitor. The authors wish to acknowledge the support of Mr. M. J. Brenner of NASA Ames Dryden Flight Research Facility and Dr. L. J. Huttsell of the U.S. Air Force Flight Dynamics Laboratory for coordinating with the authors during the numerical evaluation process. The authors also thank Dr. W. P. Rodden and the late Mr. J. H. Wykes for their constructive technical comments.

References

[1]Albano, E. and Rodden, W. P., "A Doublet Lattice Method for Calculating Lift Distributions on Oscillating Surfaces in Subsonic Flows," *AIAA Journal*, Vol. 7, Feb. 1969, pp. 279–285, and Vol. 7, Nov. 1969, p. 2192.

[2]Stark, V. J. E., "Calculation of Aerodynamic Forces on Two Oscillatory Finite Wings at Low Supersonic Mach Numbers," SAAB TN 53, Linköping, Sweden, 1964.

[3]Appa, K., "Kinematically Consistent Unsteady Aerodynamic Coefficients in Supersonic Flow," *International Journal for Numerical Methods in Engineering*, Vol. 2, No. 4, Oct.–Dec. 1970, pp. 495–507.

[4]Woodcock, D. L. and York, E. J., "A Supersonic Box Collocation Method for the Calculation of Unsteady Airforces of Tandem Surfaces," AGARD-CP-80-71, Pt. 1, April 1971.

[5]Ii, J. M., Borland, C. J., and Hogley, J. R., "Prediction of Unsteady Aerodynamic Loadings of Nonplanar Wings and Wing-Tail Configurations in Supersonic Flow; Part 1: Theoretical Development, Program Usage, and Application," Air Force Flight Dynamics Lab., TR-71-108, Pt. I, March 1972.

[6]Cunningham, A. M., "Oscillatory Supersonic Kernel Function Method for Interfering Surfaces," *Journal of Aircraft*, Vol. 11, Nov. 1974, pp. 664–670.

[7]Giesing, J. P. and Kalman, T. P., "Oscillatory Supersonic Lifting Surface Theory Using a Finite-Element Doublet Representation," AIAA Paper 75–761, May 1975.

[8]Jones, W. P. and Appa, K., "Unsteady Supersonic Aerodynamic Theory for Interfering Surfaces by the Method of Potential Gradient," *AIAA Journal*, Vol. 15, Jan. 1977, pp. 59–65 (also NASA CR-2898, Oct. 1977).

[9]Hounjet, M. H. L., "Improved Potential Gradient Method to Calculate Airloads on Oscillatory Supersonic Interfering Surfaces," *Journal of Aircraft*, Vol. 19, May 1982, pp. 390–399.

[10]Ueda, T. and Dowell, E. H., "Doublet-Point Method for Supersonic Unsteady Lifting Surfaces," *AIAA Journal*, Vol. 22, Feb. 1984, pp. 179–186.

[11]Chen, P. C. and Liu, D. D., "A Harmonic Gradient Method for Unsteady Supersonic Flow Calculations," *Journal of Aircraft*, Vol. 22, May 1985, pp. 371–379.

[12]Appa, K., "Constant Pressure Panel Method for Supersonic Unsteady Airloads Analysis," *Journal of Aircraft*, Vol. 24, Oct. 1987, pp. 696–702.

[13]Lottati, I. and Nissim, E., "Nonplanar Supersonic Three-Dimensional Oscillatory Piecewise Continuous-Kernel Function Method," *Journal of Aircraft*, Vol. 24, Jan. 1987, pp. 45–54.

[14]Appa, K. and Smith, M. J. C., "Integration of a Supersonic Unsteady Aerodynamic Code into the NASA FASTEX System," Northrop Rept. NOR-88-10, Jan. 1988.

[15]Chen, P. C. and Liu, D. D., "Unsteady Supersonic Computation of Arbitrary Wing-Body Configurations Including External Stores," AIAA Paper 88-2309, April 1988.

[16]Neill, D., Johnson, E. H., and Canfield, R., "ASTROS-A Multidisciplinary Automated Structural Design Tool," AIAA Paper 87-0713, April 1987.

[17]Maier, H. and King, S., "Transonic Flutter Model Tests; Part I: 45° Swept Wings," WADC Technical Rept. 56–214, Sept. 1957.

[18]Huttsell, L. J., private communication, Sept. 1987.

[19]Borland, C. J., "XTRAN3S—Transonic Steady and Unsteady Aerodynamics for Aeroelastic Applications, Volume I—Technical Development Summary," Air Force Wright Aeronautical Labs., TR-85-3124, Vol. I, Jan. 1986.

[20]Woodward, F. A., "An Improved Method for the Aerodynamic

Analysis of Wing-Body-Tail Configurations in Subsonic and Supersonic Flow," Part I: Theory and Applications. Part II: Computer Program Description, NASA CR-2228, May 1973.

[21]Pollock, S. J. and Huttsell, L. J., "Application of Three Unsteady Aerodynamic Load Prediction Methods," Air Force Flight Dynamics Laboratory, TR-73-147, May 1974.

[22]Mykytow, W., Olsen, J. J., and Pollock, S. J., "Application of AFFDL Unsteady Load-Prediction Methods to Interfering Surfaces," AGARD Symposium on Unsteady Aerodynamics for Aeroelastic Analyses of Interfering Surfaces, Tonsberg, Norway, AGARD-CP-80-71, Paper No. 7, 1970.

[23]Frei, D. and Moore, M., "X-29 High Angle of Attack, Flexible, Nonlinear Aerodynamic Math Model (Aero 7); Data Tables," Grumman Aircraft Corporation Memo No. 712/ENG-M-84-161, May 1984.

[24]Yamamoto, T. G., Wong, H. W., and Chung, D. K., "F-8 Oblique Wing Feasibility Study Extension-Final Report," NA-84-2097, Nov. 1984.

[25]Yates, E. C., Jr., Land, N. S., and Foughner, J. T., Jr., "Measured and Calculated Subsonic and Transonic Flutter Characteristics of a 45-deg Sweptback Wing Planform in Air and in Freon-12 in the Langley Transonic Dynamics Tunnel," NASA TN D-1616, March 1963.

[26]Yates, E. C., Jr., "AGARD Standard Aeroelastic Configurations for Dynamic Response. Candidate Configuration 1—Wing 445.6," NASA TM 100492, Aug. 1987.